Festkörper Quantenbits

Kane prosal

articles

A silicon-based nuclear spin quantum computer

B. E. Kane

Semiconductor Nanofabrication Facility, School of Physics, University of New South Wales, Sydney 2052, Australia

Quantum computers promise to exceed the computational efficiency of ordinary classical machines because quantum algorithms allow the execution of certain tasks in fewer steps. But practical implementation of these machines poses a formidable challenge. Here I present a scheme for implementing a quantum-mechanical computer. Information is encoded onto the nuclear spins of donor atoms in doped silicon electronic devices. Logical operations on individual spins are performed using externally applied electric fields, and spin measurements are made using currents of spin-polarized electrons. The realization of such a computer is dependent on future refinements of conventional silicon electronics.

Although the concept of information underlying all modern computer technology is essentially classical, physicists know that nature obeys the laws of quantum mechanics. The idea of a quantum computer has been developed theoretically over several decades to elucidate fundamental questions concerning the capabilities and

to quantum computation[11,12] circumvents the single-spin detection problem essentially by performing quantum calculations in parallel in a large number of molecules and determining the result from macroscopic magnetization measurements. The measurable signal decreases with the number of qubits, however, and scaling this

Kane scheme

semiconductors are composed primarily $I = 0$ isotopes and can in principle be purified to contain only $I = 0$ isotopes. Because of the

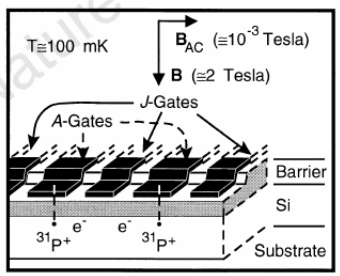

Figure 1 Illustration of two cells in a one-dimensional array containing ^{31}P donors and electrons in a Si host, separated by a barrier from metal gates on the surface. 'A gates' control the resonance frequency of the nuclear spin qubits; 'J gates' control the electron-mediated coupling between adjacent nuclear spins. The ledge over which the gates cross localizes the gate electric field in the vicinity of the donors.

Magnitude of spin interactions in Si:^{31}P

The size of the interactions between spins determines both the time

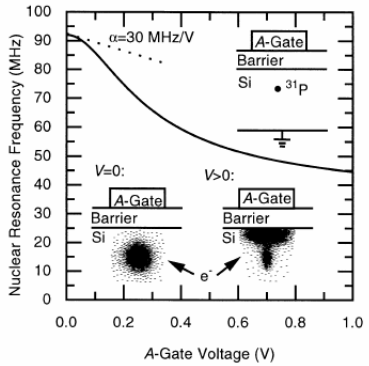

Figure 2 An electric field applied to an *A* gate pulls the electron wavefunction away from the donor and towards the barrier, reducing the hyperfine interaction and the resonance frequency of the nucleus. The donor nucleus–electron system is a voltage-controlled oscillator with a tuning parameter α of the order of 30 MHz V^{-1}.

Motivation: Solid state QC with quantum dots (Kane proposal)

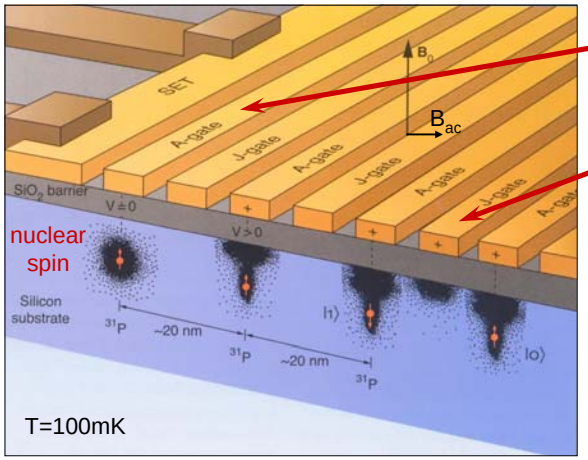

Control of strength of hyperfine interaction
⇨ Voltage controlled oscillator

Switch on/off: Electron mediated coupling between nuclear spins

B_{ac} flips nuclear spins at resonance

Readout:
nuclear spin
⇨ electron spin
⇨ orbital wavefunction
⇨ capacitance meas.

B. E. Kane, Nature **393**, 133 (1998)

Fabrication studies

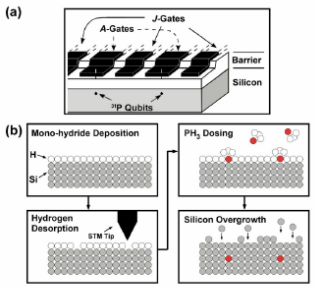

FIG. 1. (Color) A schematic of the process to fabricate the Kane architecture. (a) Detail of the Kane quantum computer architecture taken from Ref. 7, showing two phosphorus qubits in a linear array, incorporated into isotopically pure ^{28}Si and isolated from surface metal *A* and *J* gates by an insulating barrier. (b) A process to fabricate an array of phosphorus qubits in silicon. A low defect density Si(001)2×1 surface is passivated with a monolayer of hydrogen. A STM tip is used to selectively desorb hydrogen, exposing silicon on an atomic scale permitting only one phosphine molecule to adsorb at each of the required sites. Low-temperature silicon overgrowth encapsulates the phosphorus.

in this step is to ensure that the phosphorus atoms incorporate into the silicon crystal and remain in their ordered

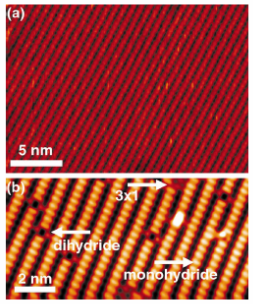

FIG. 2. (Color) Preparation of clean and hydrogen terminated surfaces. (a) Filled state STM image of a clean, very low defect density Si(001)2×1 surface. This image was acquired at a sample bias of −1.0 V and a tunneling current of 0.4 nA. (b) Fully hydrogen terminated Si(001)2×1 surface. Image acquired at −2.5 V and 0.4 nA. The surface is almost entirely 2×1 monohydride, with sites of 1×1 dihydride and 3×1 trihydride also identified.

"bean" shaped protrusions in this filled state image correspond to the charge overlap of the electrons in the dangling bonds on each silicon surface atom giving rise to a weak π-bond. These dangling bonds make the surface reactive, al-

Realization of a novel deterministic source of single atomic ions

Wolfgang Schnitzler, Norbert M. Linke, Johannes Eble, Ferdinand Schmidt-Kaler, Kilian Singer

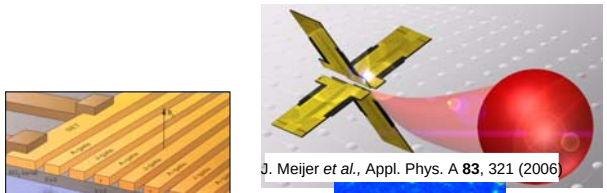

J. Meijer *et al.*, Appl. Phys. A **83**, 321 (2006)

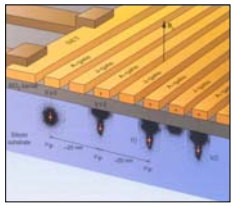

Solid state QC with quantum dots
B. E. Kane, Nature **393**, 133 (1998)

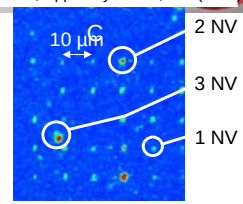

color centers in diamond
cooperation with: J. Meijer (Bochum),
J. Wrachtrup, F.Jelezko (Stuttgart)

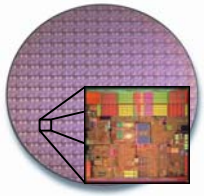

Reduction of the threshold voltage of Semiconductor devices
T. Shinada et.al., Nature 437, 1128 (2005)

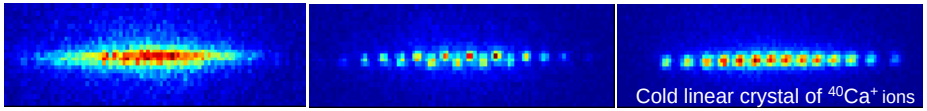

Trap Setup

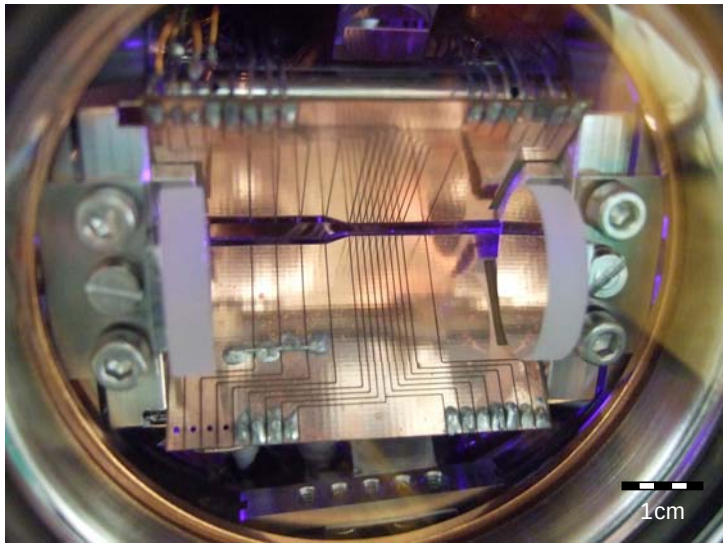

Segmented Paul Trap as perfect point source for laser cooled ions

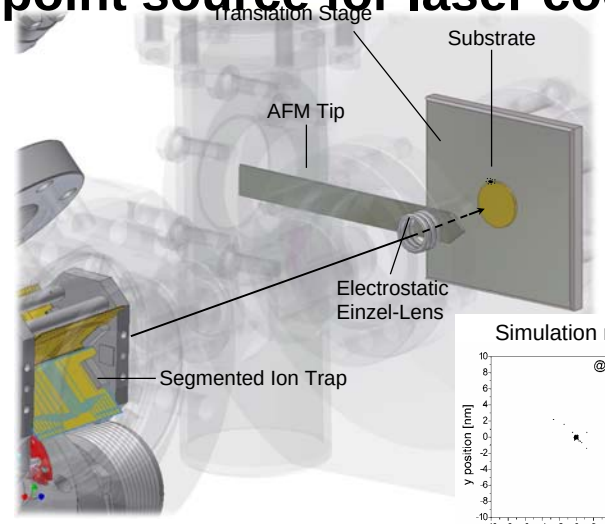

+ top-down method
+ only singly charged ions are needed
+ independant of dopant atom
+ low energy (<1keV)
+ nm resolution

- limited throughput
- only shallow implantation

Simulation results of focussing @T=100µK

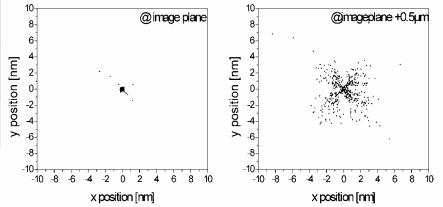

J. Meijer *et al.*, Appl. Phys. A **83**, 321 (2006)

Deterministic extraction of ion crystals and detection with EM tube

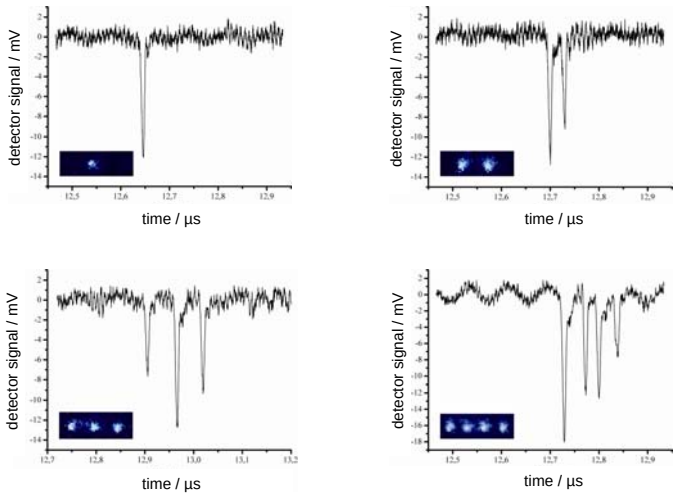

Einzelspin auslesen

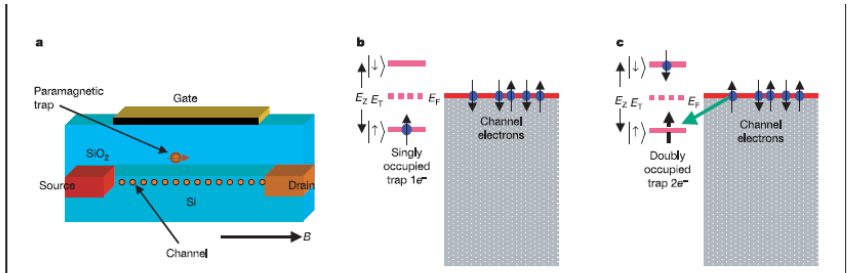

Figure 1 The mechanism for spin-to-charge conversion. **a**, A single paramagnetic trap, situated in a standard commercial n-channel Si FET that constitutes our sample. **b**, The Zeeman-split trap level relative to the FET channel Fermi level. The Fermi level would have to shift towards the upper Zeeman level to reach 50% occupation probability. (The singly occupied state should actually be down-shifted by the Coulomb correlation energy U, not shown.) **c**, If the spin flips under ESR, the lower Zeeman level can become filled, producing the doubly occupied trap.

Einzelspin auslesen

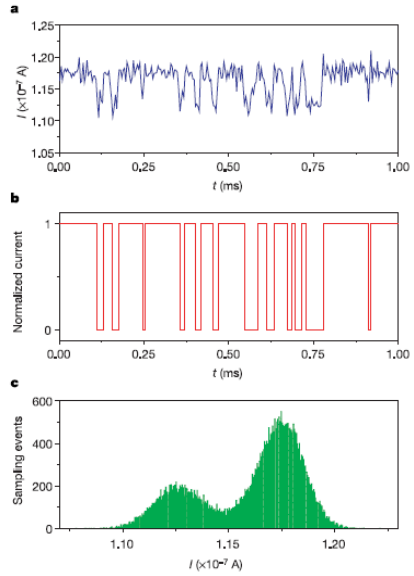

Figure 3 Detailed analysis of the random telegraph signal. **a**, The raw random telegraph data displayed for a time interval of 1 ms. **b**, An algorithm for detection of abrupt changes is applied to the raw data to reconstruct the two RTS levels. This procedure reduces the statistical errors due to noise. **c**, A histogram of the time-domain data. The large and small peaks represent the empty and filled trap states, respectively.

Farbzentern in Diamant

Motivation: NV colour centers (Universität Stuttgart)

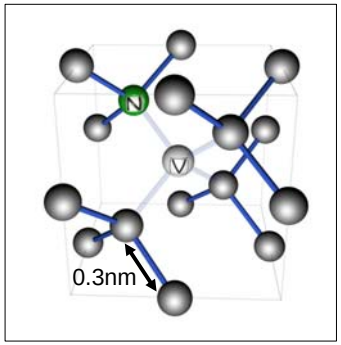

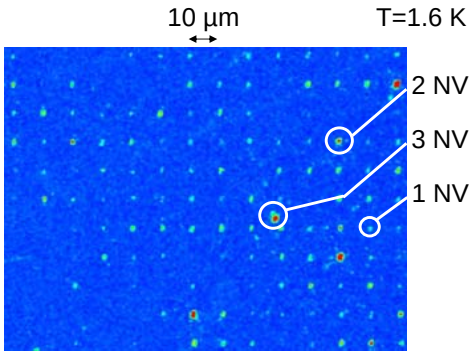

2 MeV: spot size 300nm

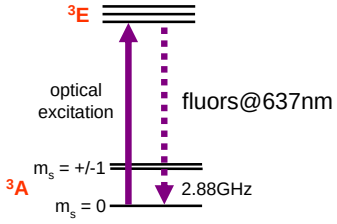

	[NV] color center
Wavelength	637 nm
Linewidth	24 MHz
Dipole Moment	1×10^{-29} Cm

Prof. J. Wrachtrup / F. Jelezko (Universität Stuttgart)
J. Meijer (RUBION, Bochum)

REPORTS

Multipartite Entanglement Among Single Spins in Diamond

P. Neumann,[1]* N. Mizuochi,[2]* F. Rempp,[1] P. Hemmer,[3] H. Watanabe,[4] S. Yamasaki,[5] V. Jacques,[1] T. Gaebel,[1] F. Jelezko,[1] J. Wrachtrup[1]†

Robust entanglement at room temperature is a necessary requirement for practical applications in quantum technology. We demonstrate the creation of bipartite- and tripartite-entangled quantum states in a small quantum register consisting of individual ^{13}C nuclei in a diamond lattice. Individual nuclear spins are controlled via their hyperfine coupling to a single electron at a nitrogen-vacancy defect center. Quantum correlations are of high quality and persist on a millisecond time scale even at room temperature, which is adequate for sophisticated quantum operations.

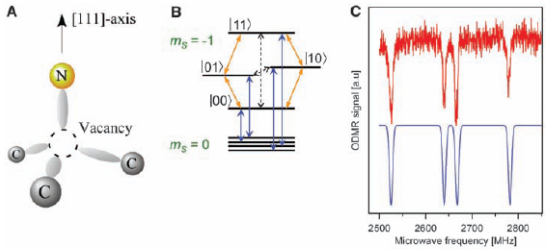

Fig. 1. (**A**) Atomic structure of the NV center. The nitrogen atom, vacancy, and three nearest-neighbor carbon atoms are shown. Two of the carbon atoms are ^{13}C isotopes with nuclear spin 1/2. (**B**) Energy-level scheme of electronic ground state of the NV center. Two of three hyperfine split electron spin sublevels (m_S = 0,–1) are depicted. Allowed transitions are shown by solid arrows (blue, electron spins; orange, nuclear spins). Zero and double quantum transitions are shown as dashed arrows. For further information, see (*15*). (**C**) ODMR spectrum (red curve) showing the m_S = 0↔–1 transition. The simulated spectrum (blue curve) accounts for the hyperfine splitting of a single electron spin with two nearest-neighbor ^{13}C atoms. a.u., arbitrary units.

Table 1. Fidelity and entanglement measures for Bell, *GHZ*, and *W* states. Dashes indicate that the respective coherence measures were not calculated.

Coherence measure → Bell state ↓	Fidelity	Concurrence	Partial transpose
Ψ^+	0.80 ± 0.07	$0.65^{+0.15}_{-0.08}$	$-0.31^{+0.05}_{-0.06}$
Ψ^-	0.81 ± 0.06	0.59 ± 0.11	$-0.32^{+0.04}_{-0.05}$
Φ^+	0.98 ± 0.05	$0.96^{+0.04}_{-0.09}$	$-0.49^{+0.03}_{-0.02}$
Φ^-	0.96 ± 0.05	$0.92^{+0.07}_{-0.08}$	–0.47 ± 0.46
GHZ	0.87 ± 0.06	—	—
W	$0.85^{+0.05}_{-0.1}$	—	—

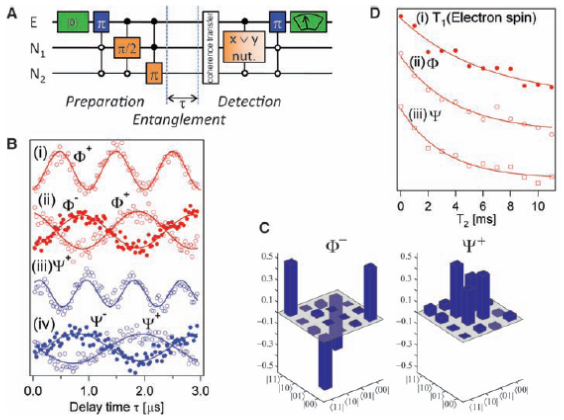

Fig. 2. (**A**) Pulse sequence for Bell state generation (Φ^-) among two nuclear spins. Spin-selective pulses are represented by squares, operating on a target qubit. Vertical lines represent logical connections. The control qubit state $|1\rangle$ and the state $|0\rangle$ are displayed as closed and open circles, respectively. For example, an open circle indicates that the pulse is applied to the target qubit if the quantum state of the controlling qubit is $|0\rangle$. Bell states evolve during time τ followed by state tomography. During six different transfer steps, the six possible coherences among the four nuclear spin states are unitarily mapped onto nuclear spin N_1. Each coherence is completely analyzed by performing two nutations (nut.) with two 90° phase-shifted rf fields. The results are the density matrix elements. (**B**) Ramsey fringes of Bell states: (i) Φ^+, (ii) Φ^+ and Φ^-, (iii) Ψ^+, and (iv) Ψ^+ and Ψ^-. The frequency offsets of rf1 ($\Delta\omega_1$), rf2 ($\Delta\omega_2$), and fitted curve (ω_{fit}) are: (i) $\Delta\omega_1$ = 0.5, $\Delta\omega_2$ = 0.5, and ω_{fit} = 1.0 MHz ≈ $\Delta\omega_1+\Delta\omega_2$; (ii) $\Delta\omega_1=0$, $\Delta\omega_2=0.5$, and $\omega_{fit}=0.5$ MHz ≈ $\Delta\omega_1+\Delta\omega_2$; (iii) $\Delta\omega_1=-0.3$, $\Delta\omega_2=1.0$, and ω_{fit} = 1.3 MHz ≈ $\Delta\omega_2-\Delta\omega_1$; and (iv) $\Delta\omega_1=0$, $\Delta\omega_2=0.4$, and ω_{fit} = 0.4 MHz ≈ $\Delta\omega_2-\Delta\omega_1$. (**C**) Density matrix reconstruction (real part) of states Φ^- and Ψ^+. Imaginary parts are found in (*15*). The high absolute values of the main off-diagonal elements (Φ^-: $|00\rangle\langle11|$, $|11\rangle\langle00|$; Ψ^+: $|10\rangle\langle01|$, $|01\rangle\langle10|$) prove that these are, in fact, entangled states and not just incoherent mixtures (otherwise, all off-diagonal elements would be zero). (**D**) Coherence time of Bell states as compared with the relaxation time of the electron T_1.

Supraleitende Qubits

Herstellung

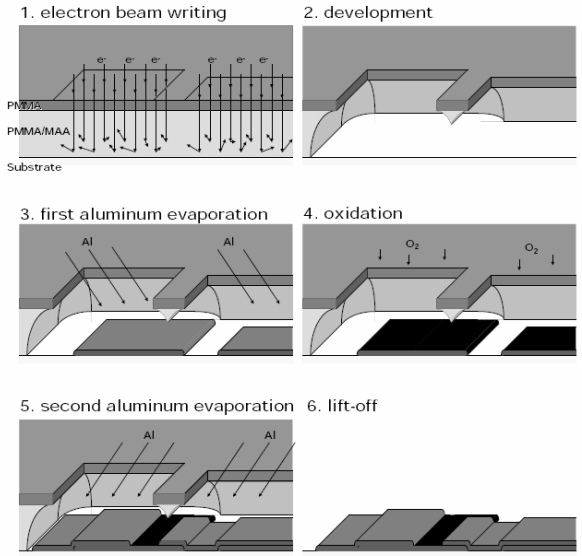

Figure 1.7: Schematic overview of the fabrication procedure.

The samples are fabricated on a silicon substrate with an insulating SiO_2 layer on top. After cleaning the substrate with acids two resist layers are spun

Josephson Kontakt

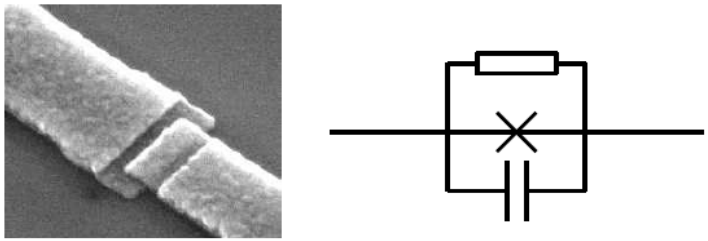

Figure 1.1: A Josephson junction consists of two superconductors which are coupled by a very thin insulating layer. Left: A scanning electron microscope image of a Josephson junction fabricated with shadow evaporation technique. Right: Resistively, capacitively shunted junction (RCSJ) model for a Josephson junction.

Josephson Kontakt

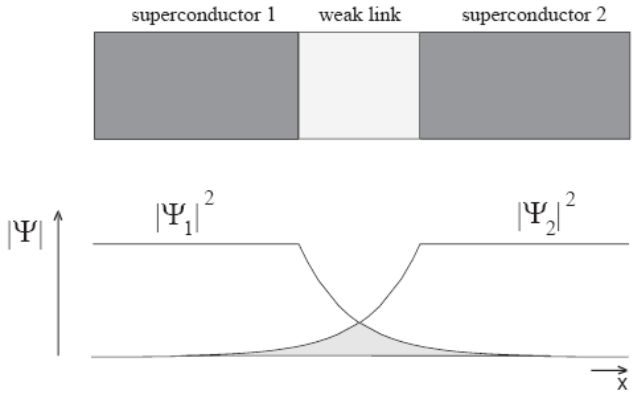

Figure 2.1: Top: A superconductor-insulator-superconductor system forming a Josephson junction. Bottom: At the boundary of a superconductor, the amplitude of the order parameter decays exponentially. This allows an overlap (shaded grey) of the two wavefunctions and provides a coupling between them.

RCSJ Modell

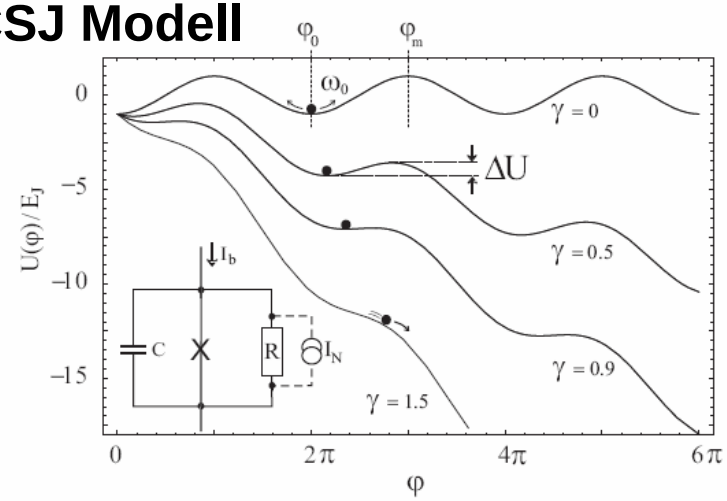

Figure 2.2: The washboard potential plotted for four different normalized bias currents γ. The virtual particle is indicated by a solid disc. For $\gamma = 0.5$, the potential barrier height ΔU is also shown. Inset: Equivalent circuit model of a Josephson junction. The Josephson supercurrent is symbolized by an X and the intrinsic capacitance and resistance are indicated as C and R, respectively. The fluctuation current source is connected by dashed lines to the resistor.

SL Qubits

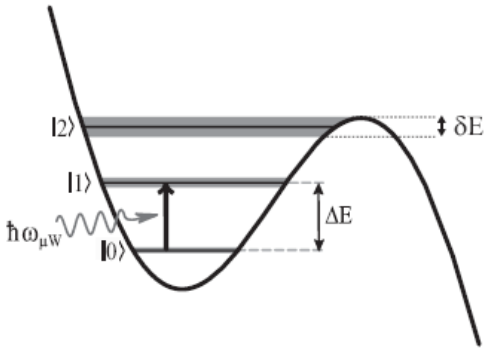

Figure 2.4: Illustration of resonant activation. The phase is activated from the ground state to the first excited state by absorbing a photon, if the photon energy $\hbar\omega_{\mathrm{RF}}$ is equal to the energy difference ΔE.

Josephson Kontakt - Schaltstrom

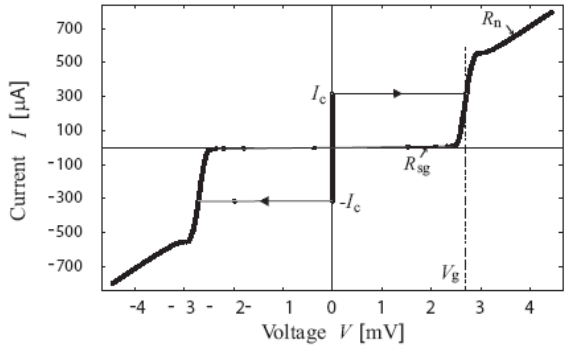

Figure 2.3: Current-voltage characteristic of a typical Josephson junction fabricated from a Nb/Al/AlO_x/Nb trilayer, measured at 20 mK temperature. Indicated by I_c is the critical current and V_g denotes the gap voltage. The slope of the curve at higher voltages displays the normal resistance $R_n \backsimeq 5.2\,\Omega$ of the barrier. Also indicated is the subgap-resistance $R_{\mathrm{sg}} \approx 400\,\Omega$.

Protokoll – Manipulieren und Auslesen

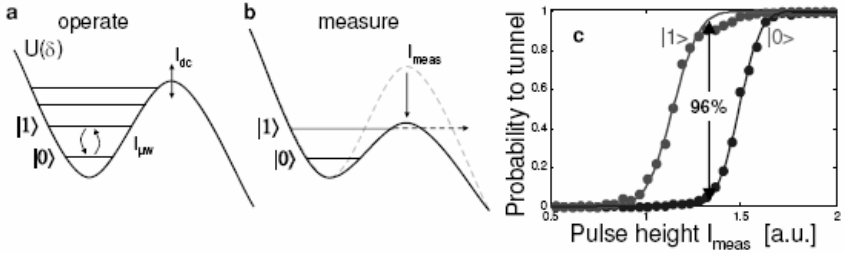

Fig. 1 (a) Plot of non-linear potential $U(\delta)$ for the Josephson phase qubit. The qubit states $|0\rangle$ and $|1\rangle$ are the two lowest eigenstates in the well. The junction bias I_{dc} is typically chosen to give 3-7 states in the well. Microwave current $I_{\mu\mathrm{w}}$ produces transitions between the qubit states. (b) Plot of potential during state measurement. The well barrier is lowered with a bias pulse I_{meas} so that the $|1\rangle$ state can rapidly tunnel. (c) Plot of tunneling probability versus I_{meas} for the states $|0\rangle$ and $|1\rangle$. The arrow indicates the optimal height of I_{meas}, which gives a fidelity of measurement close to the maximum theoretical value 96 %.

Protokoll

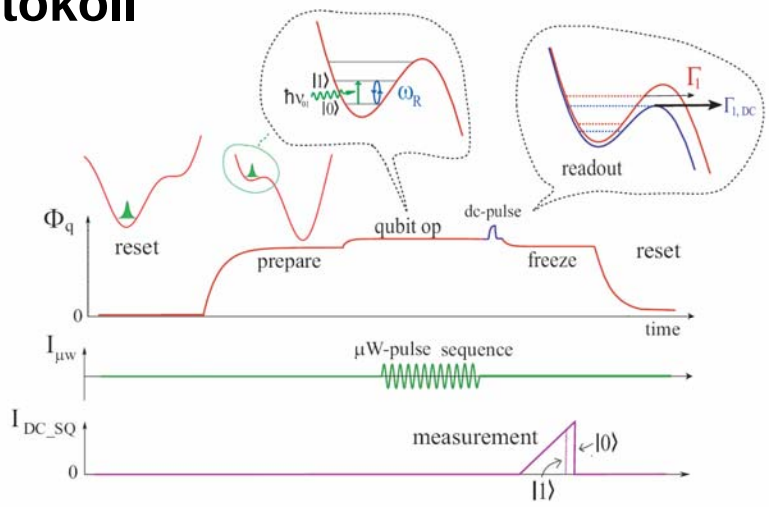

Figure 3.7: Top: Timing profile of the magnetic flux bias Φ_q applied to the qubit. Bottom: Bias current sent to the readout SQUID.

Wellenfkt im SL Qubit Potential

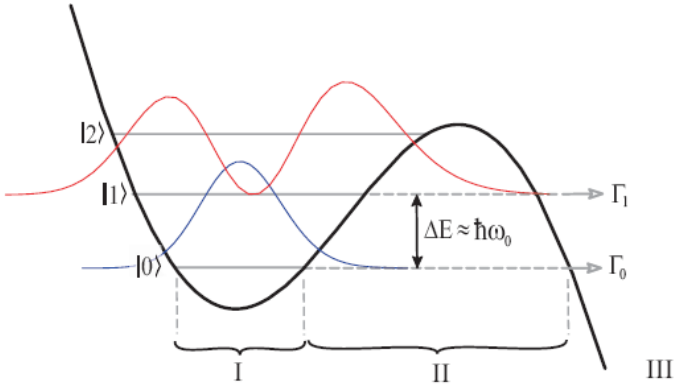

Figure 2.6: Quantum picture of the state of the Josephson phase inside the well, wherein the discrete energy levels are indicated as grey horizontal lines. Tunnelling from the excited state occurs at a rate Γ_1, which is about 1000 times larger than the tunnel rate from the ground state Γ_0 since the corresponding barrier height is reduced by the energy difference ΔE. Additionally shown is a sketch of the squared wavefunctions $|\Psi|^2$ of the ground state $|0\rangle$ and the first excited state $|1\rangle$.

Qubit Spektroskopie

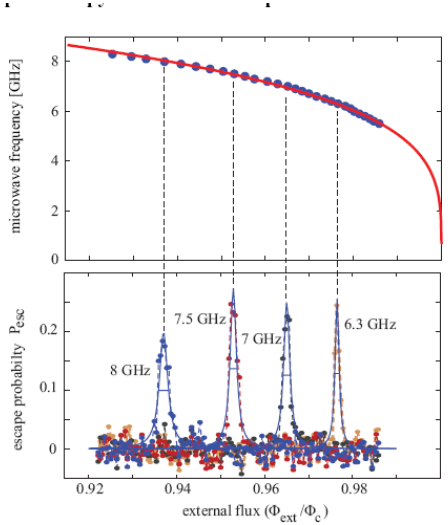

Figure 4.10: Top panel: The applied microwave frequency plotted vs. the value of external flux at which the resonance peak is found. Solid line is a fit to the small oscillation frequency $\omega_0/2\pi$, resulting in $I_c = 1.65\mu A$ and $C = 832$ fF for a fixed inductance $L = 720$ pH. Bottom panel: Resonance peaks in the escape probability, obtained by varying the external flux. Solid lines are fits to Lorentz curves. The shown resonance curves have Q-factors of ≈ 100, which are limited by the drive amplitude. Data has been taken using sample `UCSB-SiN`.

Schema

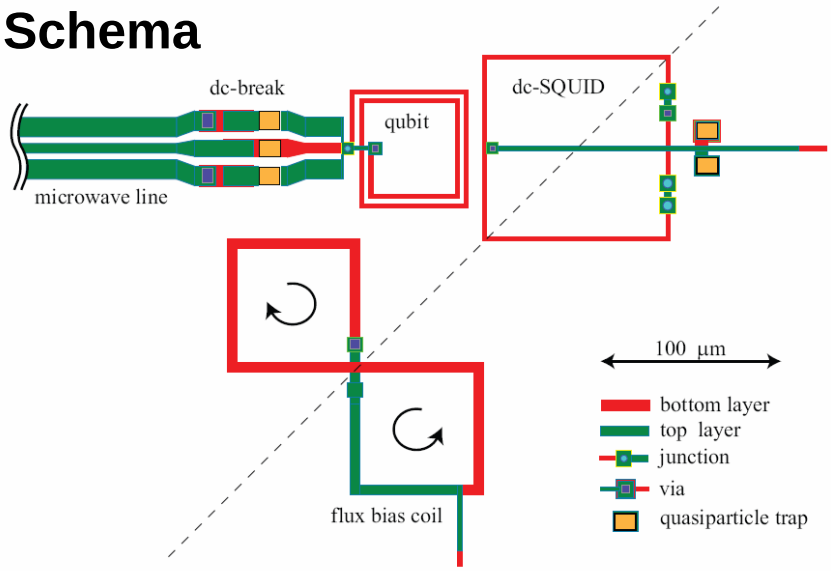

Figure 3.14: Design of sample `Hyp30` for the 30 A/cm^2 Hypres process.

Rabi Oszill.

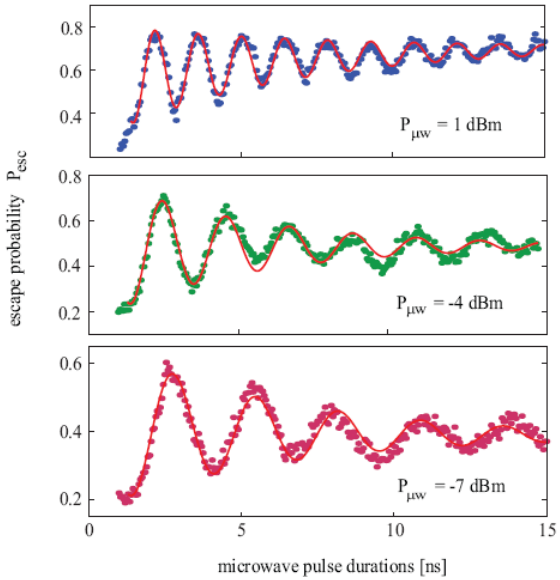

Figure 4.18: Coherent oscillations measured on sample `Hyp30S` using a drive frequency of $\omega_{\mu w}/2\pi = 13.3$ GHz and indicated power. The solid line is a fit to Eq. (4.32). Note the different vertical scale of each panel.

Spin Echo

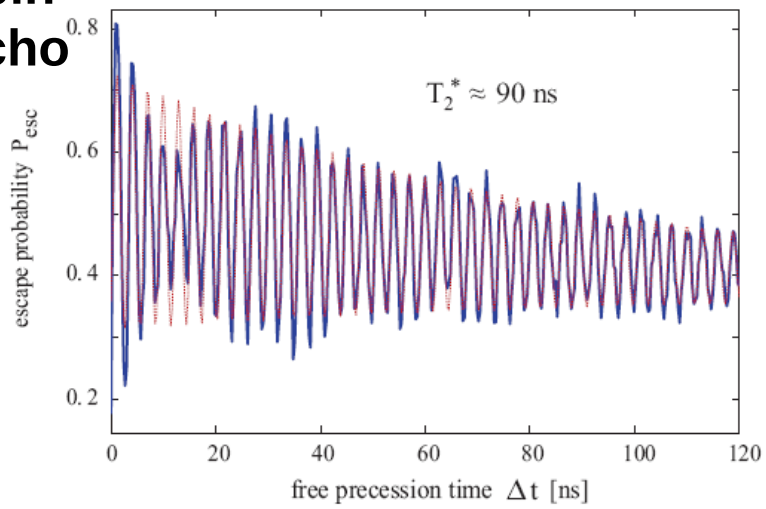

Figure 4.26: Result of an experiment to measure Ramsey oscillation using sample `UCSB-SiN`. The solid line connects measured data points, the dotted line is a fit to a sine function decaying exponentially with a time constant of $T_2^* = 90$ ns.

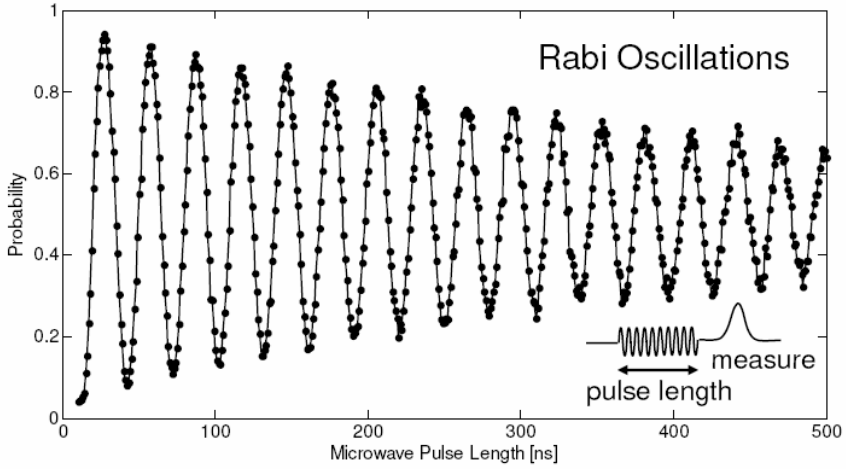

Fig. 3 Measurement of Rabi oscillations. The measurement probability of the $|1\rangle$ state is plotted versus microwave pulse length. Pulse sequence consists of a microwave pulse of variable time, tuned to the qubit transition frequency, followed by a measurement pulse, as depicted in the inset. Note that the probability is the raw data (with no corrections) coming from our experiment, which inherently has an absolute calibration. The Rabi oscillations have fidelity of about 90 %, a value reasonably close to the theoretical expectation 96 % [15]. The energy decay time for this qubit is $T_1 = 600$ ns.

Aufbau – 1 Qubit

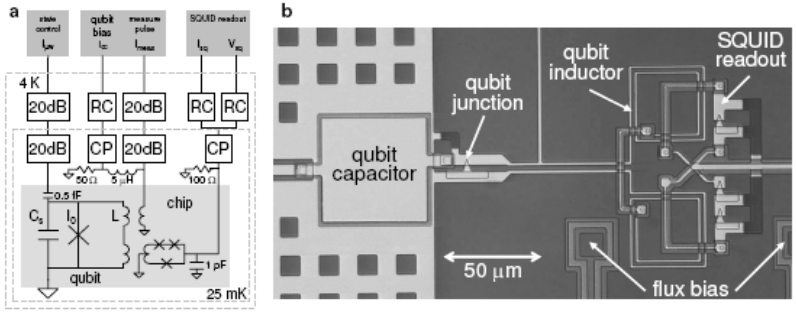

Fig. 2 (a) Schematic diagram of a phase qubit circuit and bias lines. Symbols 20 dB, RC, and CP represent 20 dB microwave attenuators, resistor-capacitor low-pass filters, and copper-powder microwave filters, respectively. The RC filters for the qubit and SQUID bias has 1 kΩ and 10 kΩ DC resistance, respectively, and a roll-off frequency $\sim$ 5 MHz. The 5 μH inductor is a custom made radio-frequency bias tee with no transmitting resonances below 1 GHz. (b) Photomicrograph of present phase qubit, showing small area ($\sim 1\,\mu m^2$) junction shunted by a parallel plate capacitor. Microwave drive line (with capacitor, not shown) comes from the left. The qubit inductor is coupled to a SQUID readout circuit in a gradiometer geometry. The flux bias lines for the qubit are symmetrically placed about the SQUID and counter-wound to inhibit flux coupling to the SQUID. The SQUID bias line exits to the right. The holes in the ground plane inhibit trapped vortices in the superconducting ground plane.

Aufbau – 2 Qubits

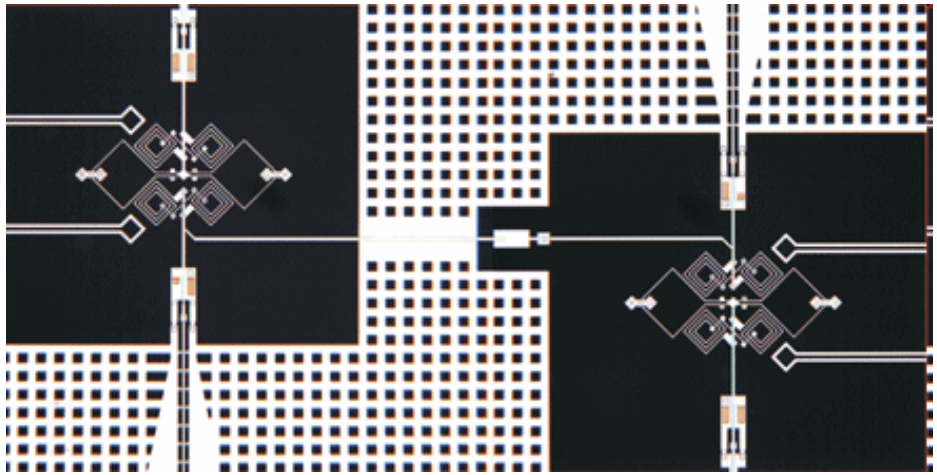

Schema 2 - Qubits

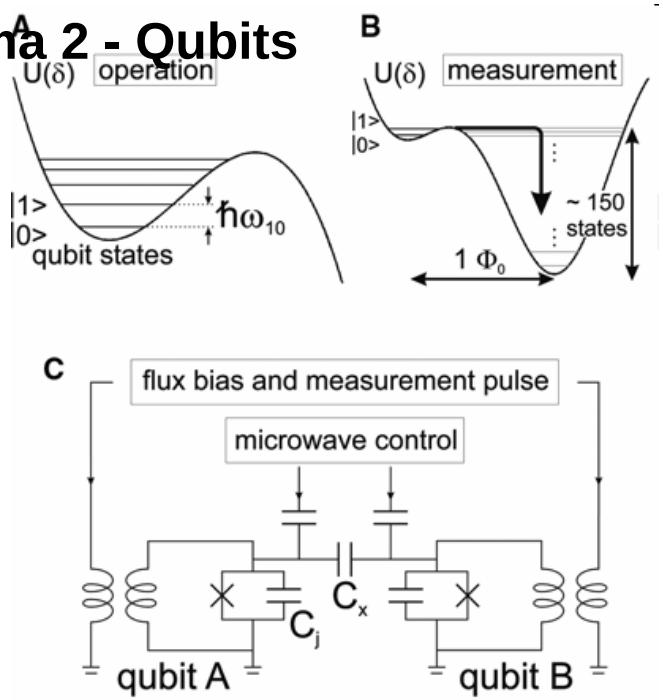

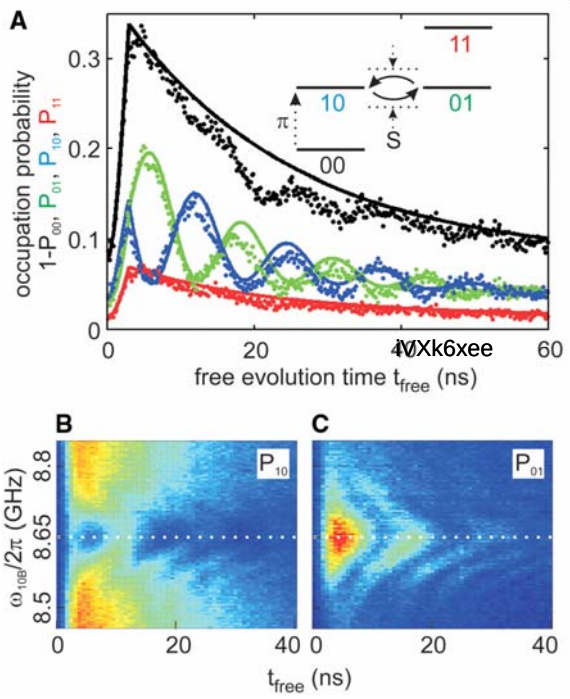

Gekoppelte Rabi-oszillationen